Epitaxial BiP$_5$O$_{14}$ layer on BiOI nanosheets enhancing the photocatalytic degradation of phenol via interfacial internal-electric-field

Zhaohui Wu [a,b], Jianfang Jing [b], Kunfeng Zhang [b], Wenlu Li [b], Jun Yang [b], Jie Shen [a], Shumin Zhang [a], Kaiqiang Xu [a], Shiying Zhang [a,*], Yongfa Zhu [b,*]

[a] Hunan Key Laboratory of Applied Environmental Photocatalysis, Changsha University, Changsha 410022, Hunan, China
[b] Department of Chemistry, Tsinghua University, Beijing 100084, China

ABSTRACT

BiOI/BiP$_5$O$_{14}$ heterostructure with enhanced interfacial internal electric field for directional charge transfer and separation effectively were constructed successfully through epitaxial BiP$_5$O$_{14}$ layer on the surface of BiOI nanosheets. Dramatical enhanced internal electric field of BiOI/BiP$_5$O$_{14}$ heterostructure was established when BiP$_5$O$_{14}$ monolayer epitaxial grow on the surface of BiOI nanosheets by adding 2% of NaH$_2$PO$_4$. As a result, this heterostructure could boost the photodegradation and mineralization of phenol. Compared to pristine BiOI nanosheets, the photocatalytic reaction constant rates of phenol over the BiOI/BiP$_5$O$_{14}$ heterostructure were elevated over 8.5 times, and the corresponding mineralization ability was also enhanced 8.9 times due to the effective and directional charges transfer and separation. This work provides an evidential proof of rational designing heterostructure via epitaxial growth, and confirms the internal electric field drive charge transfer and separation directionally for promoted photocatalytic performances.

1. Introduction

The phenolic pollutants in water were harm for environment and human health, it is emergency to remove them from the water. Recently, the photo/photoelectric-catalysis technique for pollutant removal is considered as viable and green strategy [1–5]. By using the photo/photoelectric-catalysis technique, the semiconductors are the vital roles to determine the photo/photoelectric-catalysis efficiency. And many semiconductors with unique structures have been exploited for photo/photoelectric-catalysis, particularly for photocatalysis [6–9]. Particularly, two-dimensional (2D) semiconductors have been attracted considerable interesting in photocatalysis of phenolic compounds, such as g-C$_3$N$_4$, bismuth oxyhalide (BiOX, X=Cl, Br, I), bismuth molybdate (Bi$_2$MoO$_6$) [10–13].

The BiOX have been widely studied for photocatalysis [8,14–17]. Especially, BiOI possessing excellent visible light response has frequently studied for the degradation of phenolic pollutants [18,19]. However, the too narrowed band gap, rapid recombination of charge carriers, and weaker oxidization capability of BiOI also limit its photo-degradation performances. Several strategies have been proposed to promote the charge transfer and separation for boosting the

photocatalytic performance of BiOI, such as altering the crystal phase and composition of BiOI [20–22], adjusting the exposed facets [19], elements doping [18], establishing the heterostructure [23–25]. Notably, constructing BiOI-based heterostructure with other semiconductors is assessed to be an efficient strategy, which was frequently used to promote the photocatalytic activities [25–27]. Importantly, BiOI and other components of heterostructure could build enhanced interfacial internal electric field, which can drive the charge transfer and separation efficiently, enhancing the photocatalytic activities of BiOI largely [3,28–30]. For instance, a 2D p-n heterojunctions with surface defect-engineered motif of Bi$_2$WO$_6$/BiOI nanosheets were prepared. The cascade configuration of Bi$_2$WO$_6$/BiOI heterostructure could establish internal electric field, rendering spatial separation and directional migration of charge carriers. Also, with the assistance of oxygen vacancies for surface active sites, the Bi$_2$WO$_6$/BiOI heterostructure exhibit superior photocatalytic activities of CO$_2$ reduction to CH$_4$ [29].

Regarding the constructure of BiOI-based heterostructure, the interfacial structure between BiOI and another component is vital and decisive role for the charge transfer and separation efficiency. It is necessary to establish BiOI-based heterostructure with well interface match, eliminated defects, and suppressed recombination centers of

charge carriers. Normally, BiOI-based heterostructure could be facilitated through many strategies, such as epitaxial growth, self-assembly, and anion exchange [5,31,32]. To diminish the structure disorder and depress the boundary for efficient charge transfer and separation, the epitaxial growth method is regarded as appealing strategy to construcrure BiOI-based heterostructure [32]. Despite numerous studies on the epitaxial-grow heterostructures with promoted photocatalytic activity [32–34], the distinctive epitaxial growth mechanism of establishing heterostructure, such as BiOI-based heterostructure, and the interfacial internal electric field driving the charge transfer and separation directionally still has scarcely being known.

Additionally, the superoxide radical ($\bullet O_2^-$) is the major reactive specie to photo-oxidize phenolic compounds over BiOI, which is unable to mineralize phenol predominantly or completely [35], which is still being the critical hazards for the environments and human life. Thus, raising up the mineralization ability of BiOI-based heterostructure is vital and meaningful. Photogenerated holes (h^+) have been demonstrated as critical reactive species to improve mineralization ability of phenolic compounds [23]. Thus, it is necessary to establish epitaxial heterostructure of BiOI-based nanosheets with other hole-rich semiconductors. Bismuth phosphate (such as, $BiPO_4$), as typical hole-rich semiconductor, has been considered as appealing candidate [23].

Herein, we studied the $BiOI/BiP_5O_{14}$ heterostructure construction via epitaxial growth for the phenol removal. The epitaxial growth mechanism of conducting $BiOI/BiP_5O_{14}$ heterostructure with proper interface match and the interfacial internal electric field variation of the heterostructure were illustrated by altering the concentration of NaH_2PO_4, reaction time, and temperature. Furthermore, the photocatalytic performances and mineralization ability of the $BiOI/BiP_5O_{14}$ heterostructure were also examined. During this photocatalytic process, the directional charge transfer and separation of $BiOI/BiP_5O_{14}$ heterostructure driven by the internal electric field was elucidated.

2. Experimental

2.1. Synthesis of BiOI nanosheets

The BiOI nanosheets synthesis was followed the previous report with slightly modification [32]. That was, 1 mmol $Bi(NO_3)_3$.5 H_2O were added into 25 mL mannitol (0.1 mM) under ultrasonication to form transparent homogenous solution. Then, 1 mL of NaI (1 M) were dropwise added into the above solution to form black suspension. The suspension was transferred to Teflon-lined autoclave reactor with volume of 50 mL after stirring 30 min under room temperature, and the reactor was maintained at 160 °C for 3 h. Cooling the reactor down naturally, the resultants were collected, washed, and dried for further application.

2.2. Epitaxial growth of BiOI/BiP$_5$O$_{14}$ nanosheets

0.5 mmol of the resultant BiOI nanosheets were redispersed into 30 mL of water ultrasonically for 30 min. Then, different volume of NaH_2PO_4 (0.1 M) were slowly dropped into the BiOI suspension under vigorous stirring. The well-dispersed resultants were further transferred into Teflon-lined autoclave reactor (volume of 50 mL) and kept at 180 °C for 24 h in oven. Similarly, the resultants were collected, washed, and dried. The molar percentage of added NaH_2PO_4 to BiOI is 1%, 2%, 3%, 4%, 7%, and 12%, which is highly dependent on the volume of NaH_2PO_4. Additionally, the reaction time and temperature were also varied. Detailly, the reaction time was altered from 4 h to 36 h, when fixing 2% of NaH_2PO_4 and reaction temperature at 180 °C. And the reaction temperature was varied from 120° to 180°C at fixed reaction time of 24 h and 2% of NaH_2PO_4.

2.3. Characterization

The X-ray diffractometer (Rigaku) were used to measure the powder X-ray diffraction (XRD) patterns of all samples. Scanning electron microscopy (SEM, Hitachi SU-8010), transmission electron microscopy (TEM, Hitachi HT7700) and high-resolution TEM (HRTEM) images were used to record the morphologies and intrinsic structure of the prepared products. Atomic force microscopy (AFM) images and Kelvin probe force microscope (KPFM) technique for different samples were conducted on Multiple Single-Molecule Force Spectroscopy (Cypher VRS, Oxford Instruments). UV–vis diffuse reflectance spectra (DRS) of the resulted products were performed on a UV-Vis spectrophotometer (Hitachi U-3900). Raman Microscope (LabRAM HR, Jobin Yvon) with an excitation wavelength of 632.8 nm were employed to record the Raman shifts of different samples. Thermo Fisher Spectroscope (Escalab 250 Xi) was recorded the X-ray photoelectron spectroscopy (XPS) of some samples. A fluorescence spectrophotometer (Edinburgh F900) with an excitation wavelength at 295 nm was employed to record the photoluminescence (PL) spectra. And the time-resolved transient PL spectroscopy of different samples were performed on fluorescence spectrophotometer (Edinburgh, FLS1000). The surface photovoltage (SPV) measurements were conducted with a home-built instrument as previously reported [36]. The reactive oxygen species of $\bullet O_2^-$ and hydroxyl radical ($\bullet OH$) were detected by electron paramagnetic resonance (EPR, MS-5000) technique. For this detection, 5,5-dimethyl-1-dimethy-N-oxide (DMPO) was used. And, DMPO-$\bullet O_2^-$ and DMPO-$\bullet OH$ were measured in methanol and aqueous solution, respectively. Electrochemical characterizations of the resultants including Mott-Schottky plot, electrochemical impedance spectroscopy (EIS), and photocurrent measurement were performed on the electrochemical workstation (CHI 660E, China) in a 0.5 M Na_2SO_4 solution. In the electrochemical measurement, three electrodes system including Ag/AgCl electrode, Pt sheet, and FTO glass coated with different samples were used as reference electrode, counter electrode, and working electrode, respectively.

2.4. Photocatalytic activity

The photocatalytic performances of different samples were carried out on the photocatalytic instrument (XPA-7, Nanjing Xujiang Electromechanical Factory), and the constructure of this photocatalytic instrument was showed in Fig. S1. The photocatalytic performances of different samples were evaluated by photodegrading the phenol solution under Xenon lamp (300 W) with or without a 420 nm cut-off filter for visible light or full-spectra light, respectively. Typically, 20 mg of resulted photocatalysts were dispersed in 50 mL of phenol solution (10 mg/L) ultrasonically to form suspension. This suspension was stirring in the dark for 1 h to achieve equilibrium of adsorption-desorption before light turning on. After turning on the Xenon lamp, 2 mL of aliquots were withdrawn from reacted suspension at each fixed interval, the samples were removed by employing 0.22 μm Millipore filters. The concentration of resulted transparent solution was analyzed on the High-Performance Liquid Chromatography (HPLC, Prominence, Shimadzu). The intermediates and products were investigated by Liquid Chromatograph Mass Spectrometer (LC-MS, Agilent 6530 Q/TOF) analysis.

2.5. Computational details

All calculations in this study were performed by using the plane wave based periodic density functional theory (DFT) method as implemented in the Vienna Ab Initio Simulation Package (VASP) [37–39]. The electron-ion interaction of each model was described with the projector augmented wave (PAW) method [40]. The electron exchange and correlation energies were treated within the generalized gradient approximation in the Perdew-Burke-Ernzerhof functional (GGA-PBE) [39]. The plane wave basis was set up to 500 eV. The adsorption energy was calculated according to $E_{ads} = E_{X/slab} - [E_{slab} + E_X]$, where $E_{X/slab}$ is the total energy of the slab with adsorbates in its equilibrium geometry, E_X and E_{slab} are the total energy of the free adsorbates and total energy of the bare slab, respectively.
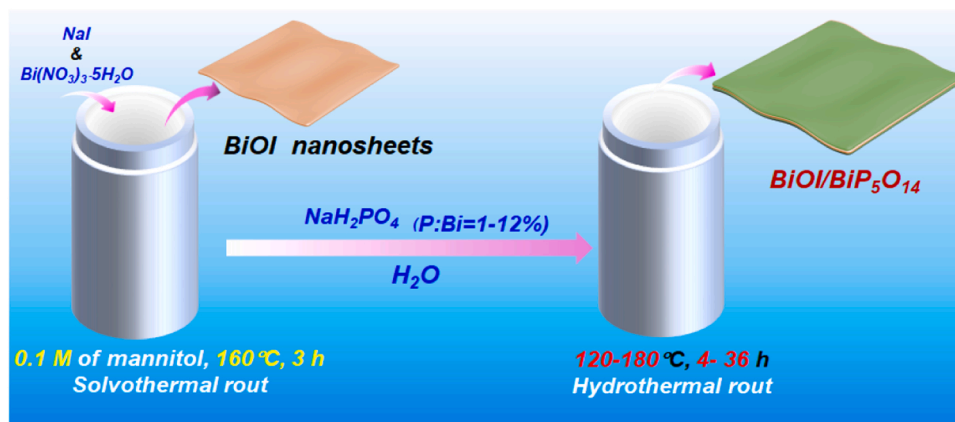
Scheme 1. The synthetic route of experiment process.
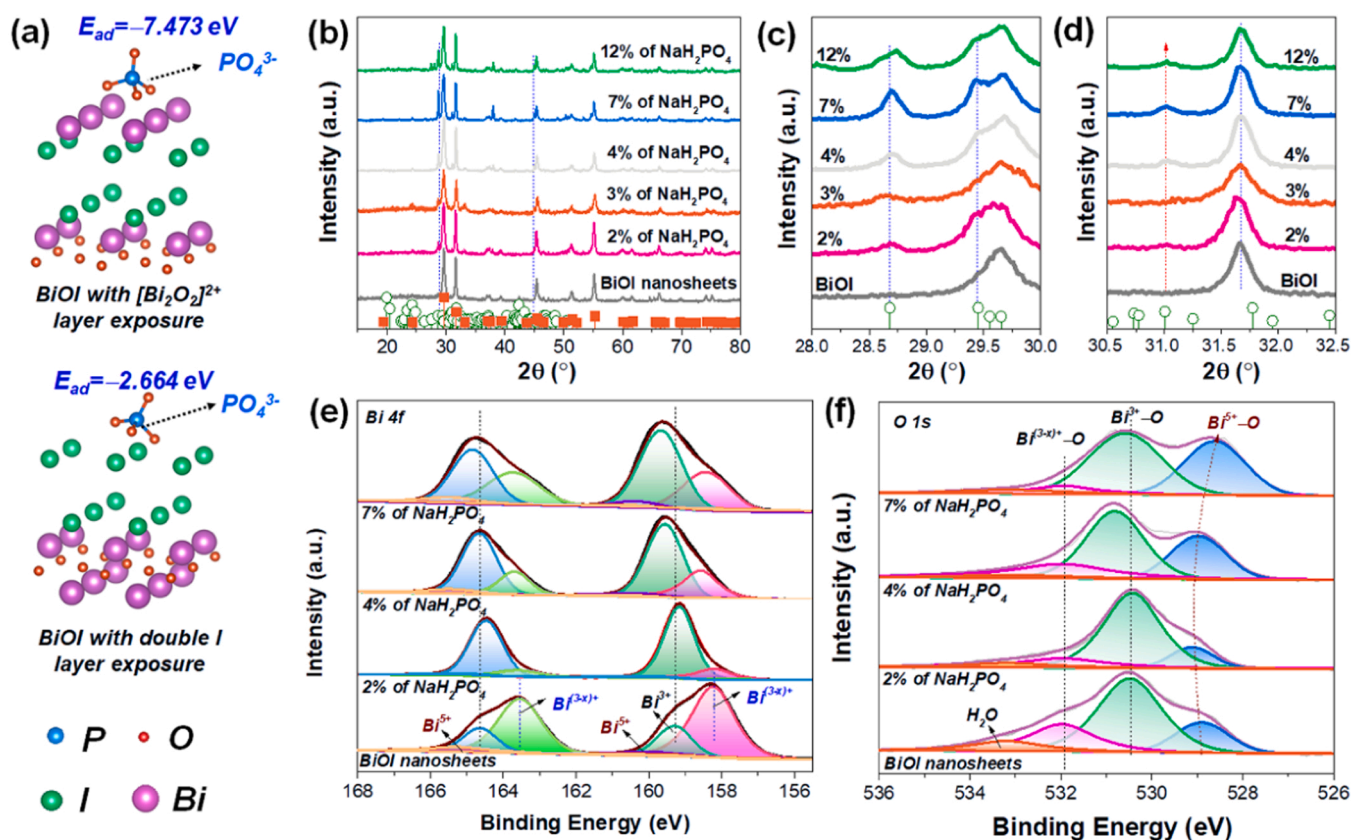

Fig. 1. (a) Surface adsorption energy comparison of BiOI with different atoms termination. (b) XRD patterns, partial enlarged XRD patterns of different samples in the range of (c) 28–30°, (d) 43–46.5° (■ BiOI (JCPDS No. 73–2062), ○ BiP_5O_{14} (JCPDS No. 36–0005)). High resolution XPS spectra of (e) Bi 4 f, (f) O 1 s of different samples.

The (001) surface of BiOI is cleaved from the bulk BiOI with symmetry of P4/nmm (129) as a $2 \times 2 \times 1$ supercell model. The defined lattice parameters of BiOI were set up according to the experiment as a $= b = 3.994$ Å, $c = 9.149$ Å, $\alpha = \beta = 90°$, $\gamma = 120°$. The symmetry of BiP_5O_{14} is P21/c with $a = 12.92$ Å, $b = 8.931$ Å, $c = 8.694$ Å, $\alpha = \gamma = 90°$, $\beta = 90.538°$.

3. Results and discussion

3.1. Epitaxial growth of BiP_5O_{14} on the surface of BiOI nanosheets

The crystal structures of BiOI and BiP_5O_{14} were showed, and both

band structure of each bulk materials was calculated, as showed in Fig. S2 and Table S1. Theoretically, the bulk BiOI and BiP_5O_{14} could form Type-I heterostructure to promote charge transfer [41]. The pristine BiOI nanosheets and BiOI/BiP_5O_{14} nanosheets were prepared through two-step solvothermal and hydrothermal routes, all synthetic process has been illustrated in Scheme 1.

Before synthesis, the surface adsorption energy of phosphate group on BiOI with different terminated atoms were examined through simulation. According to Fig. 1a, the phosphate adsorbed on the surface of BiOI terminated with $[Bi_2O_2]^{2+}$ present lower surface adsorption energy of -7.473 eV, compared with that of BiOI with double iodine ions termination (-2.664 eV). These simulated results suggested that the
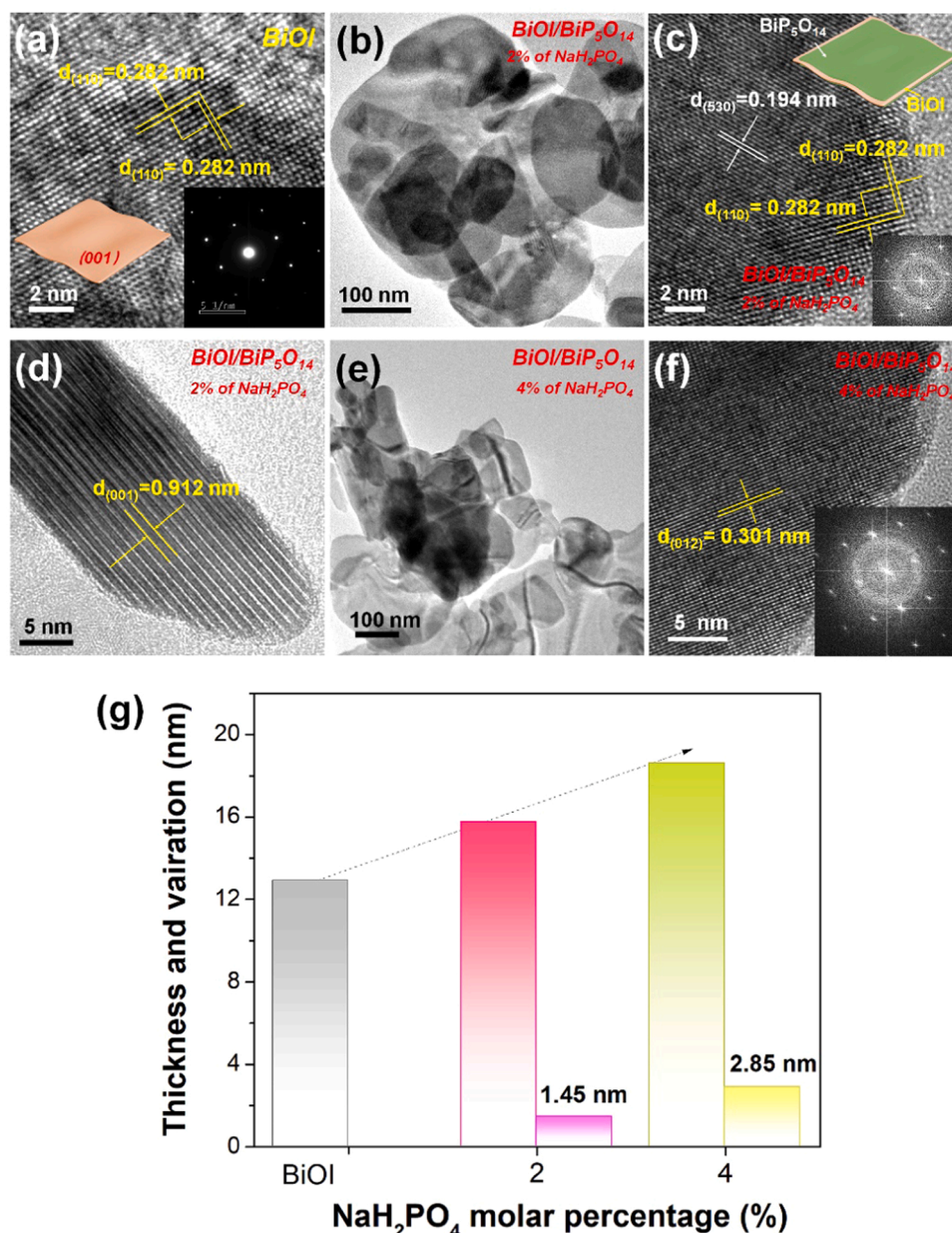
Fig. 2. (a) HRTEM of BiOI nanosheets (inset with SAED patterns and illustrated BiOI), (b) TEM, (c) HRTEM and (d) lateral HRTEM images of BiOI/BiP$_5$O$_{14}$ by adding 2% of NaH$_2$PO$_4$ (inset with represented BiOI/BiP$_5$O$_{14}$). (e) TEM, (f) HRTEM images (inset with corresponding FFT patterns) of BiOI/BiP$_5$O$_{14}$ by adding 4% of NaH$_2$PO$_4$. (g) The thickness and thickness variation of different samples.

phosphate groups are preferable to adsorb and epitaxial grow on the surface of BiOI with [Bi$_2$O$_2$]$^{2+}$ termination [42]. The epitaxial BiP$_5$O$_{14}$ layer on the surface of different BiOI nanosheets prepared by altering the molar ratio of Bi^{3+} and I$^−$ were also validated that BiOI nanosheets with [Bi$_2$O$_2$]$^{2+}$ termination was of benefit to the epitaxial growth of BiP$_5$O$_{14}$ (Fig. S3a and S3b).

The XRD patterns of prepared BiOI nanosheets were well-indexed to tetragonal BiOI (JCPDS No. 73–2062). After epitaxial growth of BiP$_5$O$_{14}$, all the main characteristic peaks of BiOI were retained (Fig. 1b). But, some characteristic peaks indexed to monoclinic BiP$_5$O$_{14}$ (JCPDS No. 36–0005) were observed (Figs. 1c and 1d). For instance, 2θ located at 28.68° and 31.00° respective indexed to the (022) and (312) planes of BiP$_5$O$_{14}$ were observed, revealing the formation of BiP$_5$O$_{14}$. And, the intensity of these characteristic peaks was gradually increased when elevating the molar percentage of NaH$_2$PO$_4$ from 2% to 12%, suggesting that the percentage of BiP$_5$O$_{14}$ was raised up.

With the increasing molar percentage of BiP$_5$O$_{14}$, the chemical state and surface structure of the resulted BiOI/BiP$_5$O$_{14}$ nanosheets were also changed significantly, comparing with pristine BiOI nanosheets (Figs. 1e and 1f). The high-resolution Bi 4 f spectrum of initial BiOI nanosheets could be deconvoluted into six peaks [43]. Two peaks at banding energy of 164.64 and 159.21 eV were ascribed to Bi 4 f$_{5/2}$ and Bi 4 f$_{7/2}$, respectively, indicating the form of Bi^{3+} [42]. Besides, two satellited peaks with dramatic higher intensity at lower binding energies of 163.54 and 158.23 eV were attributed to the Bi$^{(3−x)+}$ states caused by the surface defects of oxygen vacancies (Fig. 1e) [44,45]. Notably, other two peaks with relative lower intensity at higher binding energy of 165.3 and 160.05 eV assigned to Bi^{5+} states were also observed, which was in consistent with the previous report [43]. In the high-resolution O 1 s spectrum of BiOI, the dominant peak at 530.48 eV, and other weak intensity peaks at 528.90, 531.98, and 533.19 eV were respective ascribed to Bi^{3+}−O, Bi^{5+}−O, Bi$^{(3−x)+}$−O, and surface adsorbed hydroxyl groups

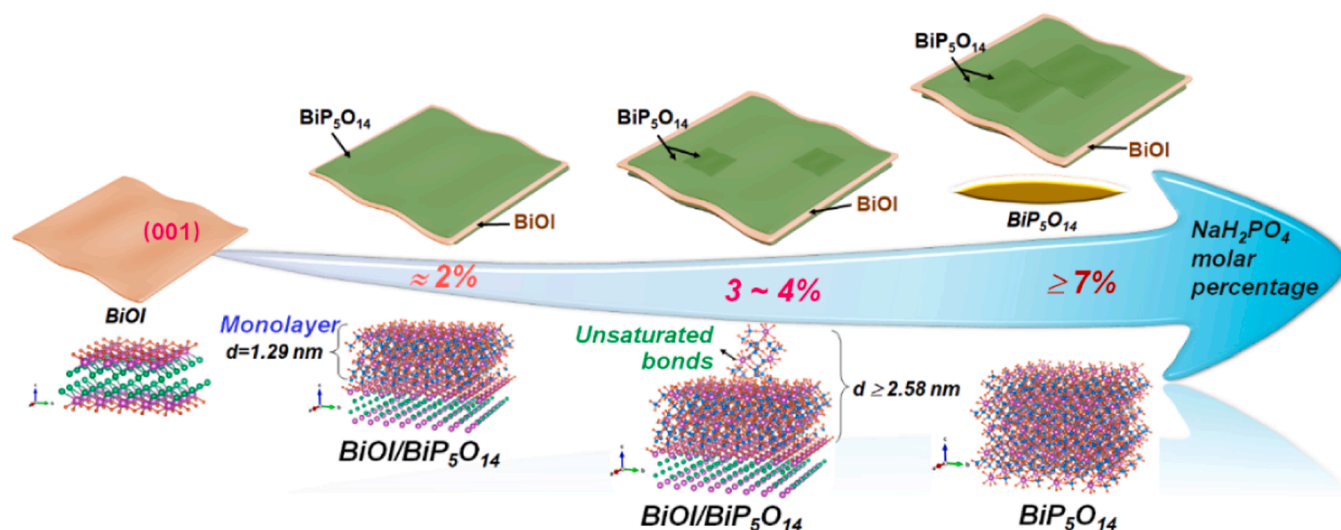**Fig. 3.** Schematic illustration of the epitaxial growth of BiP_5O_{14} on surface of BiOI nanosheets.

[43], which was in accordance with its Bi 4 f spectra. When adding 2% of NaH_2PO_4 to form $BiOI/BiP_5O_{14}$ heterostructure nanosheets, the peaks of Bi 4 $f_{5/2}$ and Bi 4 $f_{7/2}$ were slightly shifted to the lower binding energy, suggesting that Bi^{3+} state in BiOI may receive charges from the epitaxial-grow phosphate-rich groups. Furthermore, the concentration of the surface defects was diminished dramatically, and the Bi^{5+} states almost vanished, indicating that the defect-lack structure of resulted $BiOI/BiP_5O_{14}$ heterostructure (Figs. 1e and 1f). However, when elevating the molar percentage of NaH_2PO_4 over 4%, the proportion of these peaks assigned to Bi^{3+} and $Bi^{(3-x)+}$ states was increasing gradually, the peaks of Bi^{3+} states were shifted toward to higher binding energy. These observations suggested that the defects concentration increased, the charges of bismuth ions were redistributed to the increasing epitaxial-grow phosphate-rich groups, massive surface unsaturated bonds were remained [44]. Accordingly, the percentage of $Bi^{5+}-O$ in the resulted heterostructures was increased, reflecting the percentage of phosphate-rich groups was increased (Fig. 1f), which also was confirmed by the high-resolution P 2p spectra and Raman spectra (Fig. S3c to S3g).

The morphology and structure variation of pristine BiOI nanosheets and resulted $BiOI/BiP_5O_{14}$ nanosheets were showed in Fig. S4, S5 and Fig. 2. Apparently, the pristine BiOI is nanosheets (Fig. S4a, S5a-b). And according to the HRTEM images, the clear and continuous interplanar lattice fringes spacing of 0.282 nm assigned to (110) planes of BiOI were observed (Fig. 2a). Furthermore, the clear selected area electron diffraction (SAED) patterns and lateral lattice spacing of 0.912 nm assigned to (001) atomic planes of BiOI demonstrated that the BiOI nanosheets were major exposed with (001) facet (Fig. 2a, Fig. S5c). After epitaxial growth of BiP_5O_{14} (by adding 2% of NaH_2PO_4), the resulted $BiOI/BiP_5O_{14}$ heterostructure still maintained sheet-like morphology (Fig. 2b, S4b). And, clear interplanar lattice fringes spacing of 0.282 nm assigned to (110) planes of BiOI were also observed at the edge of nanosheets. Meanwhile, other continuous and definite lattice fringes spacing of 0.194 nm assigned to (530) atomic planes of BiP_5O_{14} were also observed on approaching center of the nanosheets. The images clearly verified the formation of $BiOI/BiP_5O_{14}$ heterostructure through epitaxial growth and the BiP_5O_{14} grew on the (001) facet of BiOI (Fig. 2c). In the lateral HRTEM image, only clear lattice fringes spacing of 0.912 nm assigned to (001) atomic planes of BiOI were observed, also confirming the BiP_5O_{14} grew on the (001) facet of BiOI nanosheets (Fig. 2d). When continuously increasing the NaH_2PO_4 concentration to 4%, the sheet-like morphology and predominate (001) facets of BiOI could be maintained (Figs. 2e-2f, Fig. S4d). However, when further increasing the concentration of NaH_2PO_4 over 7%, the resulted products

containing $BiOI/BiP_5O_{14}$ heterostructure and rod-like BiP_5O_{14} were obtained (Fig. S4e and S4f). With increasing the concentration of NaH_2PO_4, the thickness of resulted $BiOI/BiP_5O_{14}$ was increasing successively. That was, the thickness was increased by 1.45 ± 0.51, and 2.85 ± 0.60 nm for $BiOI/BiP_5O_{14}$ heterostructure nanosheets obtained by adding 2% and 4% of NaH_2PO_4, respectively, compared to initial pristine BiOI nanosheets (Fig. 2g and Fig. S4). According to the crystal structure of BiP_5O_{14} (Table S1), the increased thickness was corresponding to the monolayer or double layers of BiP_5O_{14}. Additionally, the crystallinity of generated $BiOI/BiP_5O_{14}$ heterostructure nanosheets was greatly dependent on the reaction temperature and time (Fig. S10 and S11). Reaction temperature of 180 °C and time of 24 h were the optimum conditions for constructing $BiOI/BiP_5O_{14}$ heterostructure.

Herein, based on the above results, the epitaxial BiP_5O_{14} layers on BiOI nanosheets for $BiOI/BiP_5O_{14}$ heterostructure were illustrated (Fig. 3). The pristine (001) facets of BiOI terminated with $[Bi_2O_2]^{2+}$ provide lower surface adsorption energy, which is favorable for the adsorption and epitaxial growth of phosphate-rich groups. At lower molar percentage of NaH_2PO_4 (2% of NaH_2PO_4), the $BiOI/BiP_5O_{14}$ heterostructure with monolayer of BiP_5O_{14} were established. This BiP_5O_{14} monolayer on the BiOI nanosheets could diminish the surface defects of pristine BiOI nanosheets. When continuous increasing the molar percentage of NaH_2PO_4 (3–4% of NaH_2PO_4), the excessive NaH_2PO_4 contributes to the continuous growth of BiP_5O_{14}. However, the resulted BiP_5O_{14} layers probably is unable to form complete bilayer on the surface of BiOI, remaining massive unsaturated bonds. Further increasing the concentration NaH_2PO_4 (over 7% of NaH_2PO_4), the resultants containing $BiOI/BiP_5O_{14}$ heterostructure and homogenous-nucleated BiP_5O_{14} micro-rods were obtained.

3.2. Interfacial internal electric field of BiOI/BiP₅O₁₄ nanosheets

The work function (Φ) of BiOI and BiP_5O_{14} were calculated (Fig. 4a and b). In comparison to BiOI ($\Phi_{BiOI}=4.32$ eV), the BiP_5O_{14} possess work function of $\Phi_{BiP5O14}= 4.08$ eV (Fig. 4a and b). When the BiP_5O_{14} was contacted with BiOI, the band edge of BiP_5O_{14} should bend upward, hindering the photogenerated electrons transfer to the BiOI, resulting in hole-rich interface. Whereas, the band edge of BiOI bend downward, leading to the electron-rich at the interface. Theoretically, the interfacial internal electric field could be conducted between the BiOI and BiP_5O_{14} after contacting, and the direction of the interfacial internal electric field is from BiP_5O_{14} to BiOI. Hence, the direction of interfacial internal electric field of $BiOI/BiP_5O_{14}$ heterostructure was also calculated through the first-principles calculation of charge density difference of
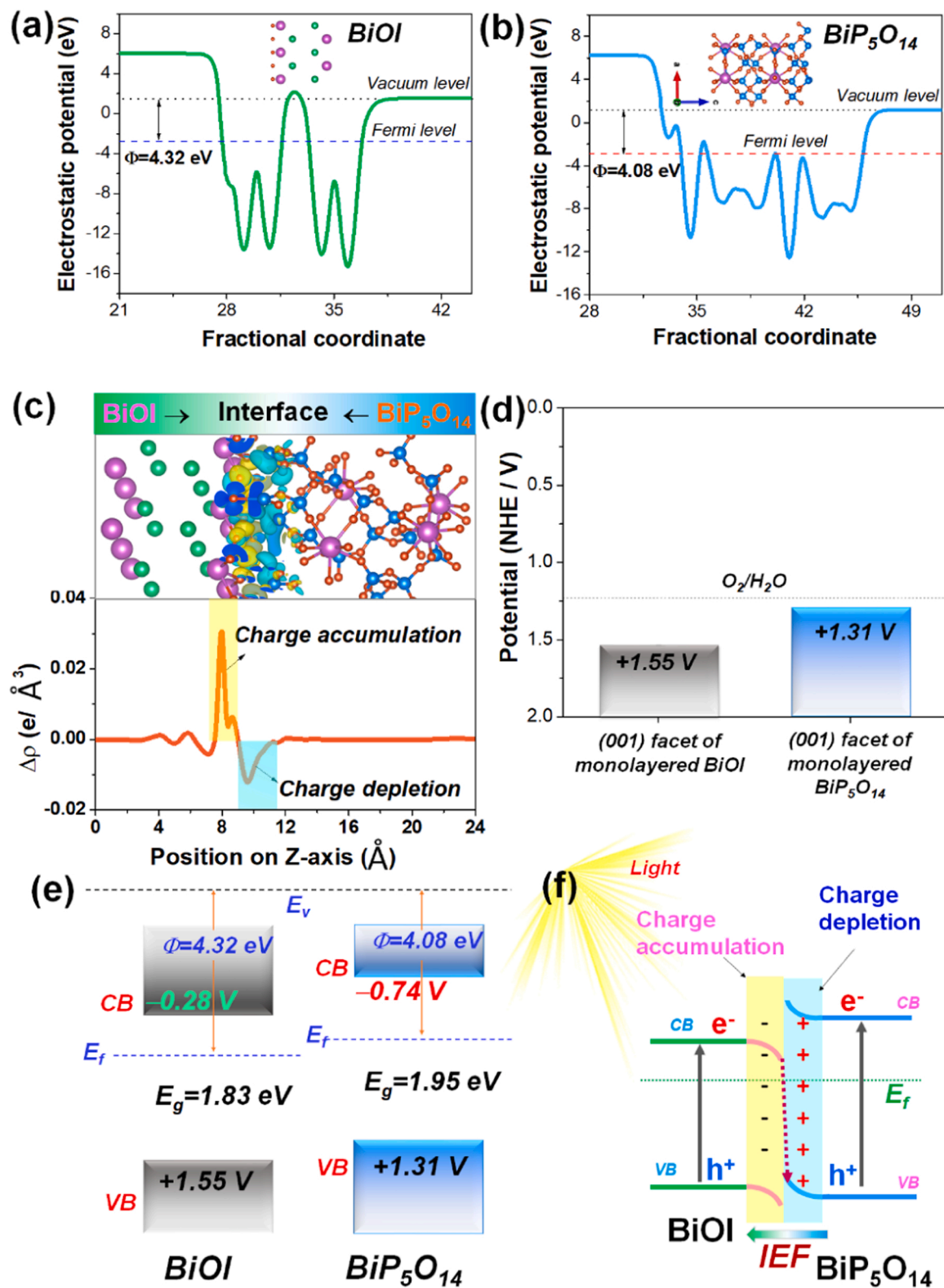
Fig. 4. Work function of (a) BiOI and (b) BiP_5O_{14}. (c) Charge density difference ($\Delta\rho = \rho_{heterojunction} - \rho_{BiOI} - \rho_{BiP5O14}$) with the corresponding planar average of the induced charge density difference and schematic energy band diagrams showing charge transfer pathway for $BiOI/BiP_5O_{14}$. (d) Calculated VBM positions corresponding to the (001) surfaces of both monolayered BiOI and BiP_5O_{14}. (e) Illustration of band structure of BiOI and BiP_5O_{14} (E_v, E_f, Φ, CB and VB are vacuum energy, Fermi energy, work function, conduction band and valence band, respectively). (f) Schematic energy band diagrams showing charge transfer pathway of $BiOI/BiP_5O_{14}$.
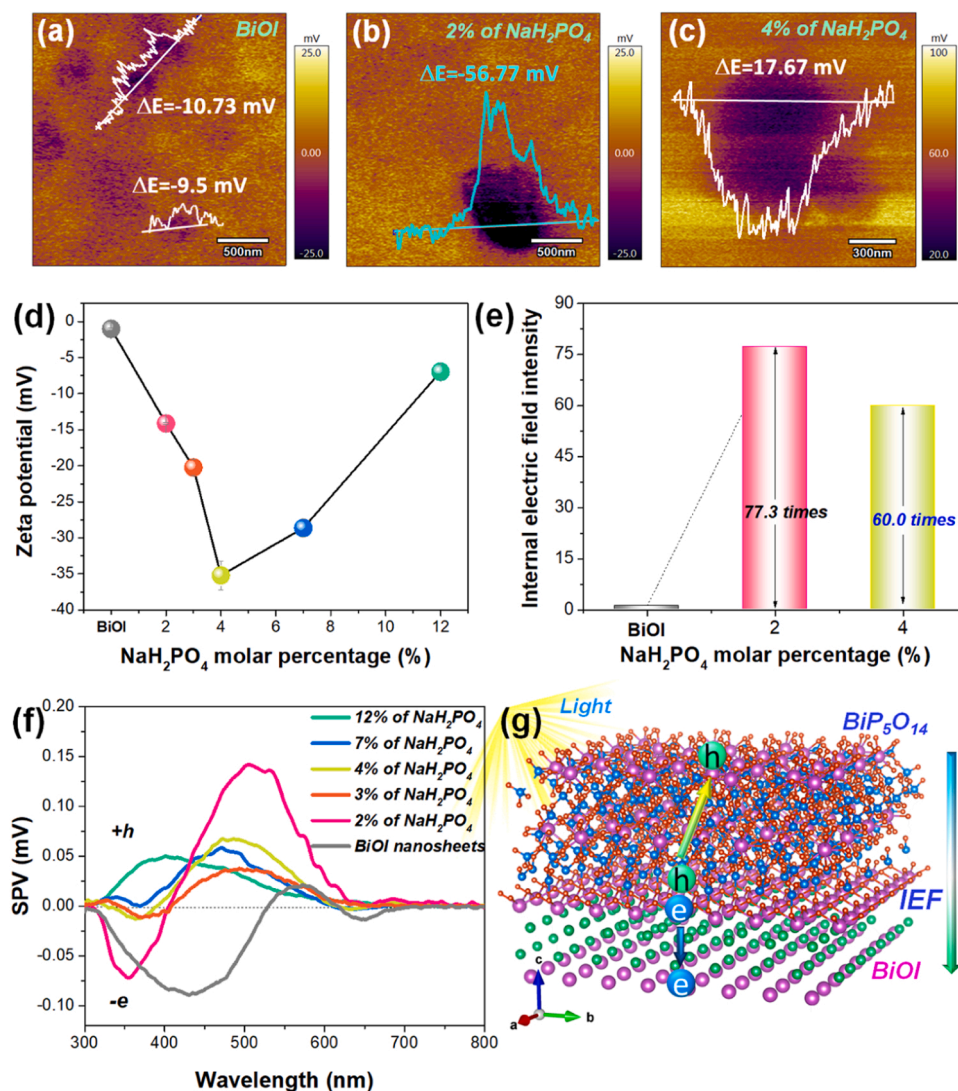
Fig. 5. KPFM images of (a) BiOI, BiOI/BiP$_5$O$_{14}$ obtained by adding (b) 2% and (c) 4% of NaH$_2$PO$_4$. (d) Zeta potential of different samples, and (e) internal electric filed intensity comparison of different samples, (f) SPV spectra of different samples. (g) Illustration scheme of charge transfer in the BiOI/BiP$_5$O$_{14}$ heterostructure with BiP$_5$O$_{14}$ monolayer.

BiOI/BiP$_5$O$_{14}$ heterostructure. The theoretical model of BiOI/BiP$_5$O$_{14}$ heterostructure was established by emphasis of the interface construction where both (001) facet surface of BiOI and BiP$_5$O$_{14}$ were selected in contact due to the lattice match. The direction of the interfacial internal electric field was obtained by subtracting the electronic charge of BiOI and BiP$_5$O$_{14}$ from the calculated charge density difference of BiOI/BiP$_5$O$_{14}$ heterostructure (Fig. 4c). Here, the charge redistribution of BiOI/BiP$_5$O$_{14}$ heterostructure is plane-averaged along the z-axis direction. The charge depletion and charge accumulation respective located at the interface of BiOI/BiP$_5$O$_{14}$ suggested that the interfacial strong interaction was conducted between these two materials, causing charge redistribution in the presence of electric dipole. Furthermore, the electric dipole induces the interfacial charge accumulation around the edge of BiOI, and charge depletion near the edge of BiP$_5$O$_{14}$ (Fig. 4c) [46]. Additionally, we tried to measure the Femi level of BiOI and BiOI/BiP$_5$O$_{14}$ nanosheets through the ultraviolet photoelectron spectroscopy (UPS), which was unsuccessfully obtained due to the poor conductivities of the resultants. Then, we considered the energetics of the heterojunction through theoretical calculations from the perspective of surface work functions of the monolayered nanosheets [42]. The valence band maximum (VBM) of the monolayered BiOI nanosheets is roughly 0.24 eV higher than that of the monolayered BiP$_5$O$_{14}$

nanosheets (Fig. 4d). Combined with the results in Fig. S7, the band structure of BiOI and BiP$_5$O$_{14}$ were present in Fig. 4e. Then, the charge transfer pathway between the BiOI and BiP$_5$O$_{14}$ were proposed in Fig. 4d. In the BiOI/BiP$_5$O$_{14}$ heterostructure, the photogenerated electrons from the conduction band (CB) of BiOI to the valence band (VB) of BiP$_5$O$_{14}$, remaining the holes at the VB of BiOI and electrons at CB of BiP$_5$O$_{14}$, which is following the Z-scheme charge transfer mechanism [46]. As a result, the photogenerated charge separation can be promoted efficiently, and the recombination of the charge carriers also is able to be suppressed.

Generally, the built interfacial internal electric field of BiOI/BiP$_5$O$_{14}$ heterostructure serve as a kinetic driving force for charge transfer and separation during the photocatalytic process. And the intensity of internal electric field in the BiOI/BiP$_5$O$_{14}$ heterostructure determines the efficiency of charge transfer and separation. Normally, the internal electric field intensity of materials is proportional to surface potential and Zeta potential [22,47]. The surface potential of BiOI and BiOI/BiP$_5$O$_{14}$ heterostructure were measured through KPFM technique (Fig. 5a-c, Fig. S8). The BiOI nanosheets with negative surface potential of -10.12 ± 0.62 eV was obtained (Fig. 5a). Comparatively, the BiOI/BiP$_5$O$_{14}$ heterostructure (by adding 2% of NaH$_2$PO$_4$) exhibited much higher negative surface potential of -56.77 ± 0.43 eV (Fig. 5b).
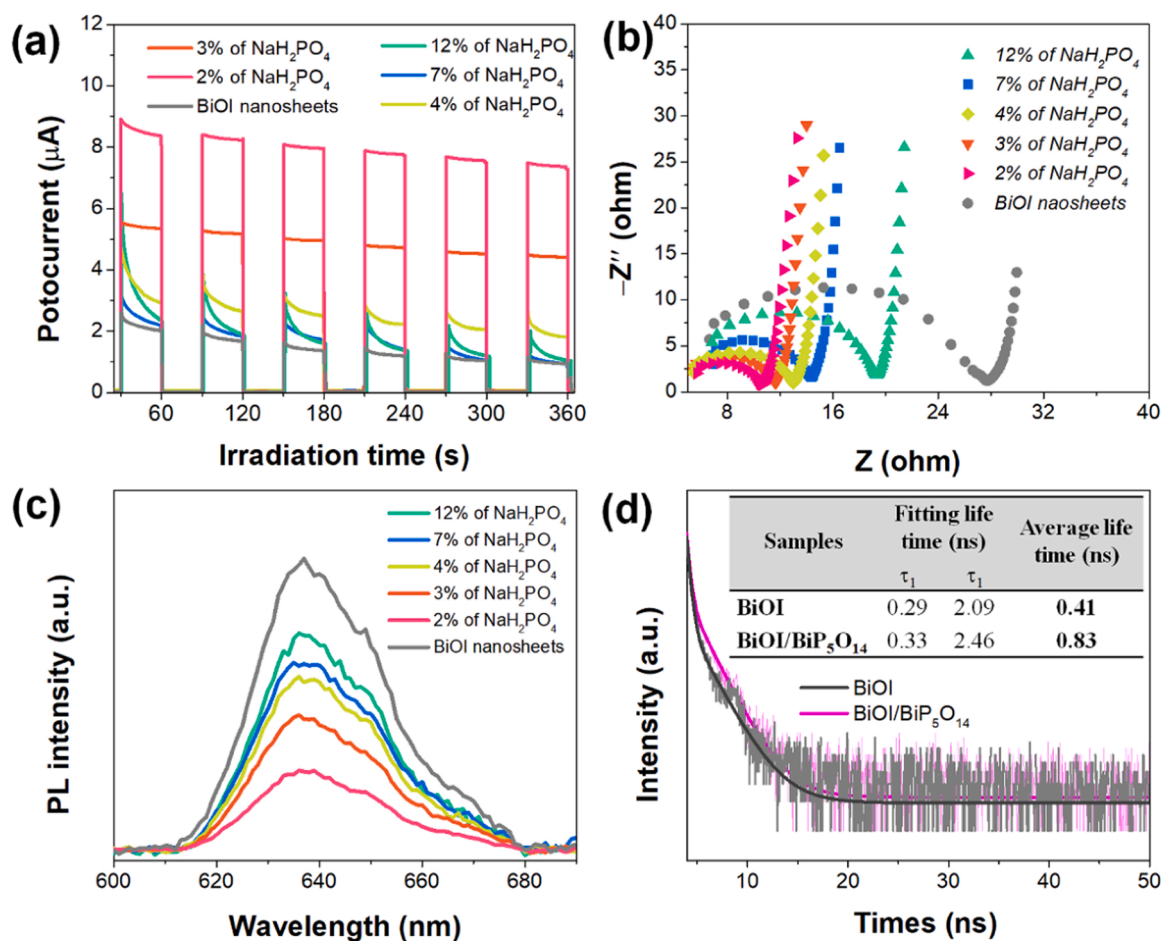
Fig. 6. (a) Photocurrent response, (b) EIS spectra, (c) steady-state PL spectra of different samples, (d) time-resolved transient PL spectroscopy comparison of BiOI and BiOI/BiP$_5$O$_{14}$ heterostructure (by adding 2% of NaH$_2$PO$_4$).

Interesting, surface potential of BiOI/BiP$_5$O$_{14}$ heterostructure obtained by adding 4% of NaH$_2$PO$_4$ were reversed to lower surface potential of 17.67 ± 1.26 eV positively (Fig. 5c). Meanwhile, the Zeta potential of different samples were examined, which showed the "V" type as increasing the concentration of NaH$_2$PO$_4$ (Fig. 5d). The Zeta potential of resulted BiOI/BiP$_5$O$_{14}$ heterostructure was continuously decreased until increasing the molar percentage of NaH$_2$PO$_4$ over 4% when starting from the approximate 0 mV of BiOI nanosheets. As a result, the BiOI/BiP$_5$O$_{14}$ heterostructure with monolayer (by adding 2% of NaH$_2$PO$_4$) possessed the highest internal electric field intensity, which was 77.3 times higher than that of pristine BiOI nanosheets, and 1.29 times than that of BiOI/BiP$_5$O$_{14}$ heterostructure obtained by adding 4% of NaH$_2$PO$_4$ (Fig. 5e).

Such enhanced internal electric filed should drive the charge separation and transfer efficiently. The SPV spectra were employed to investigate the charge transfer pathway of different samples (Fig. 5f). Obviously, the BiOI nanosheets and BiOI/BiP$_5$O$_{14}$ heterostructure with different structure present obvious difference in the charge transfer. The pristine BiOI with intrinsic internal electric filed drive the photogenerated electrons from bulk to the surface predominantly, showing negative SPV signal mainly [48]. When the BiP$_5$O$_{14}$ monolayer grow on the surface of BiOI nanosheets (by adding 2% of NaH$_2$PO$_4$), the negative SPV signal within 400 nm were reversed to positive signal in the range of 400 – 650 nm, revealing that the interfacial charge transfer follow the Z-scheme pathway [49]. However, in terms of other BiOI/BiP$_5$O$_{14}$ heterostructure obtained by adding over 3% of NaH$_2$PO$_4$, nearly positive SPV signals were harvested, indicating that the generated holes transfer from bulk to the surface predominantly in the presence of multiple-layer

BiP$_5$O$_{14}$ or excessive BiP$_5$O$_{14}$. Additionally, the SPV signal of BiOI/BiP$_5$O$_{14}$ heterostructure with BiP$_5$O$_{14}$ monolayer (by adding 2% of NaH$_2$PO$_4$) was higher than that of other BiOI/BiP$_5$O$_{14}$ heterostructure, implying that the enhanced internal electric field intensity as driving force for charge transfer was the superior one. Based on these results, the charge transfer route in BiOI/BiP$_5$O$_{14}$ heterostructure with monolayer BiP$_5$O$_{14}$ have been illustrated (Fig. 5g). In this BiOI/BiP$_5$O$_{14}$ heterostructure, the interfacial internal electric field between BiOI and BiP$_5$O$_{14}$ could drive the photogenerated holes migration to the surface of epitaxial-grow BiP$_5$O$_{14}$ monolayer, the produced electrons transfer to the surface of BiOI inversely, resulting in directional transfer and separation of charge carriers.

The charge separation of this BiOI/BiP$_5$O$_{14}$ heterostructure driven by the interfacial internal electric field also examined by the photoelectrochemical characterizations of photocurrent, EIS, PL, and time-resolved transient PL spectroscopy (Fig. 6). In comparison to BiOI and other BiOI/BiP$_5$O$_{14}$ heterostructure, the BiOI/BiP$_5$O$_{14}$ heterostructure with BiP$_5$O$_{14}$ monolayer (by adding 2% of NaH$_2$PO$_4$) exhibited superior photocurrent intensity (Fig. 6a) due to its higher charge separation dynamics. Furthermore, the smallest EIS radius and lowest PL intensity of this BiOI/BiP$_5$O$_{14}$ heterostructure (by adding 2% of NaH$_2$PO$_4$) were also observed (Fig. 6b and Fig. 6c), implying that the lowest interfacial barriers for charge transfer and charge recombination could be harvested in this BiOI/BiP$_5$O$_{14}$ heterostructure [22,48]. Regard to the life time of charge carriers, only 0.41 ns of average life time was obtained for BiOI. Comparatively, the BiOI/BiP$_5$O$_{14}$ heterostructure (by adding 2% of NaH$_2$PO$_4$) possessed 0.83 ns of charge average life time were obtained, which almost two times than that of BiOI (Fig. 6d). This longer
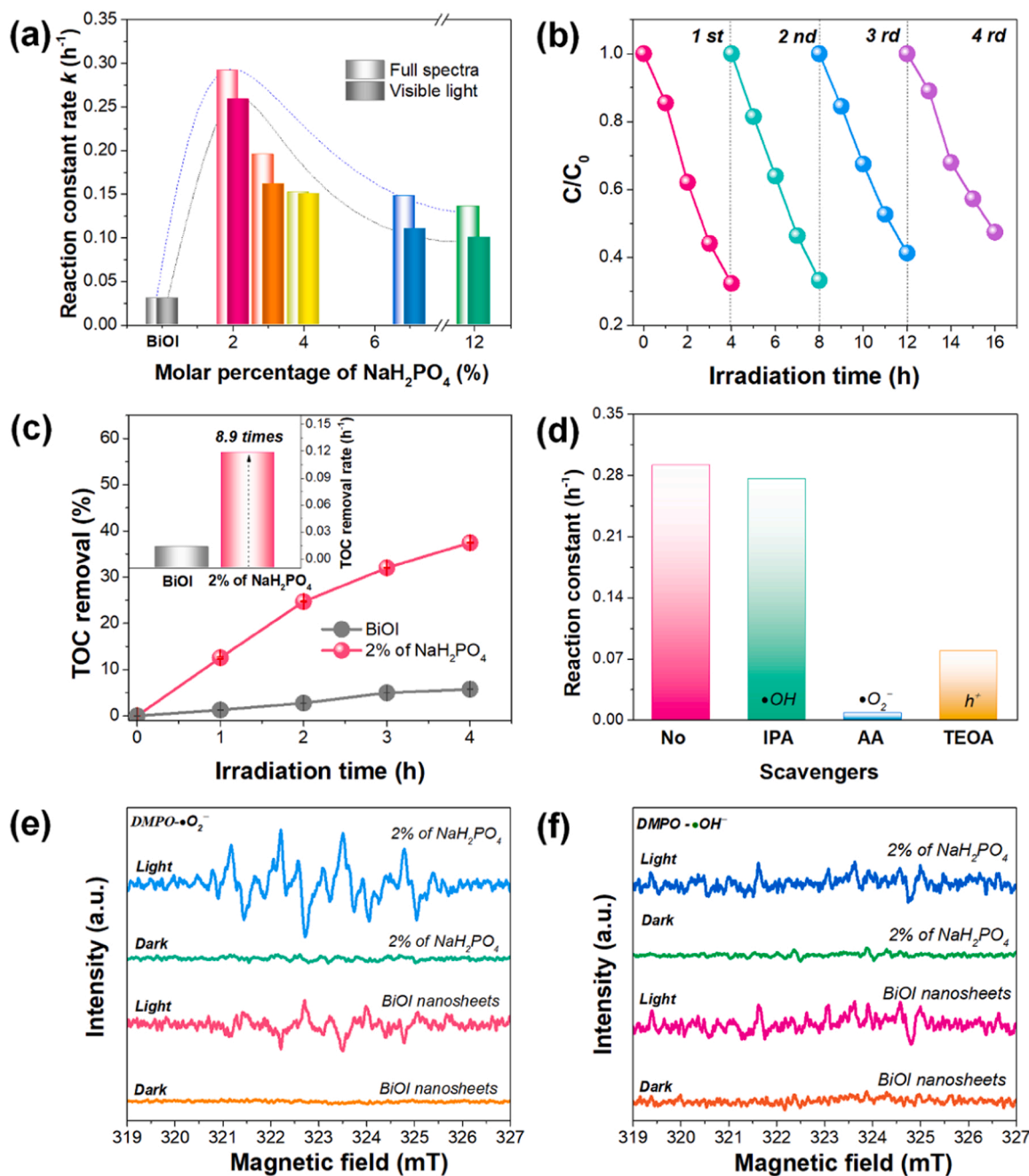
Fig. 7. (a) Reaction constant rate comparison of phenol degradation over different samples under full-light spectra and visible light, (b) photocatalytic cycling of BiOI/BiP$_5$O$_{14}$ nanosheets obtained by adding 2% of NaH$_2$PO$_4$ under full-light spectra, (c) TOC removal comparison of BiOI/BiP$_5$O$_{14}$ nanosheets and BiOI nanosheets (inset with the TOC removal rate comparison). (d) Scavenger texts of different reactive species under solar light. DMPO spin-trapping ESR spectra of different samples, (e) DMPO− •OH, and (f) DMPO− •O$_2^-$.

life time of BiOI/BiP$_5$O$_{14}$ heterostructure also demonstrated the higher charge separation efficiency [10].

3.3. Interfacial internal electric field of BiOI/BiP$_5$O$_{14}$ nanosheets enhanced the photocatalytic performance

The enhanced internal electric field of BiOI/BiP$_5$O$_{14}$ heterostructure (by adding 2% of NaH$_2$PO$_4$) drive the directional charge transfer and separation efficiently, probably resulting in excellent photocatalytic performance. Therefore, the photocatalytic performances of BiOI and different BiOI/BiP$_5$O$_{14}$ heterostructures were investigated (Fig. 7a, Fig. S9-S11). Under the full spectra, the phenol was barely removed even within 4 h by using pristine BiOI nanosheets and re-hydrothermal-treat

BiOI nanosheets (Fig. S9a). While, the BiOI/BiP$_5$O$_{14}$ heterostructure (by adding 2% of NaH$_2$PO$_4$) removed around 80% of phenol under same conditions, which is also more reactive than other BiOI/BiP$_5$O$_{14}$ heterostructure (Fig. S9a). Such similar tendency also was observed by irradiating under visible light (Fig. 7a and Fig. S9b). Compared the reaction constant rate, the BiOI/BiP$_5$O$_{14}$ heterostructure (by adding 2% of NaH$_2$PO$_4$) showed reaction constant rate of 0.292 h^{-1} and 0.260 h^{-1} under full spectra and visible light, respectively (Fig. 7a), which were almost 9.6 times and 8.5 times higher than that of BiOI nanosheets (0.030 h^{-1}). These outstanding photocatalytic activity of BiOI/BiP$_5$O$_{14}$ heterostructure (by adding 2% of NaH$_2$PO$_4$) were attributed to the superior internal electric field for charge transfer and separation efficiently. Furthermore, this BiOI/BiP$_5$O$_{14}$ heterostructure (by adding 2%
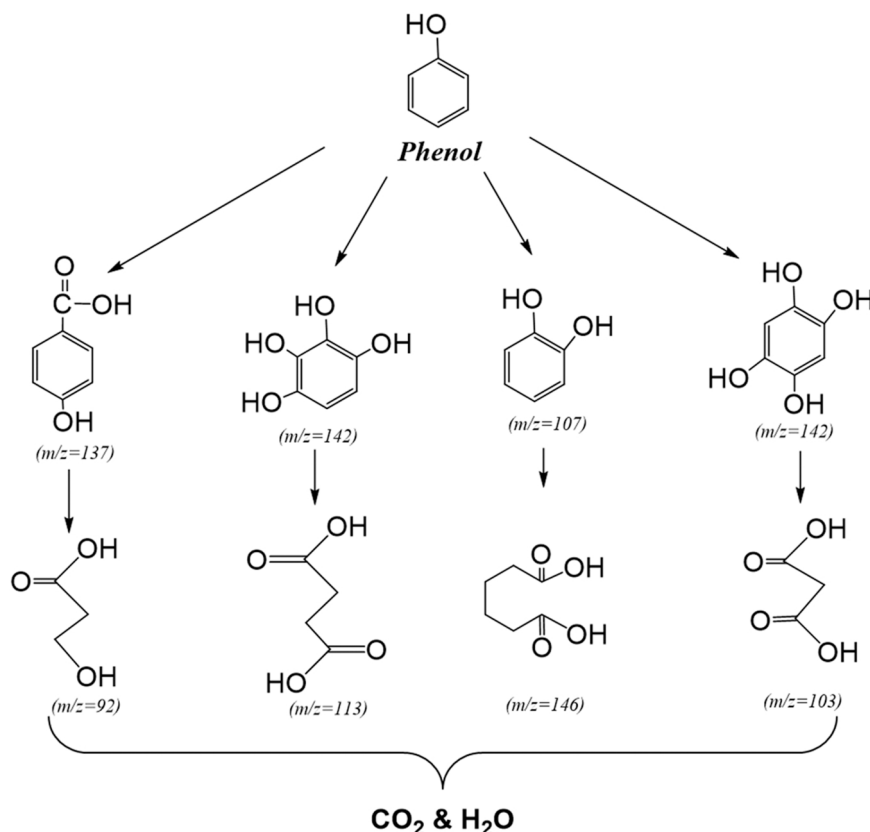
Fig. 8. Proposed reaction pathways for phenol degradation by $Bi_4O_5I_2$-$BiPO_4$ (by adding 2% of NaH_2PO_4).

of NaH_2PO_4) present excellent photocatalytic stability, according to the recycling tests and (Fig. 7b). Additionally, the TOC removal efficiency of $BiOI/BiP_5O_{14}$ heterostructure (by adding 2% of NaH_2PO_4) also was higher than that of pristine BiOI nanosheets. That was, the TOC removal rate of $BiOI/BiP_5O_{14}$ heterostructure (by adding 2% of NaH_2PO_4) was 8.9 times than that of BiOI nanosheets (Fig. 7c), revealing that the mineralization ability of the $BiOI/BiP_5O_{14}$ heterostructure was improved dramatically. Furthermore, compared with previous studies about $BiOI/BiPO_4$ heterostructure, other $BiOI/BiP_5O_{14}$ heterostructure and mechanical mixed BiOI and $BiPO_4$ (Table S2, Fig. S12, and Fig. S13) [3,23,50,51], this $BiOI/BiP_5O_{14}$ heterostructure exhibited excellent photocatalytic performances of phenol removal.

To investigate the reactive species of $BiOI/BiP_5O_{14}$ heterostructure (by adding 2% of NaH_2PO_4) during the photocatalytic process, the scavenger tests were conducted by adding IPA, AA, and TEOA as scavengers of $\bullet OH$, $\bullet O_2^-$, and h^+, respectively (Fig. S7c and Fig. 7d). Apparently, the $\bullet O_2^-$ and h^+ were the predominant reactive species of $BiOI/BiP_5O_{14}$ heterostructure during the photocatalytic process. Furthermore, the significant DMPO-$\bullet O_2^-$ signal of $BiOI/BiP_5O_{14}$ heterostructure were detected under light irradiation, while such signal of BiOI nanosheets were barely observed (Fig. 7e). Simultaneously, the DMPO-$\bullet OH$ signals were scarcely detected for both BiOI nanosheets and $BiOI/BiP_5O_{14}$ heterostructure (by adding 2% of NaH_2PO_4) (Fig. 7f). These results confirmed that the $\bullet O_2^-$ and h^+ of $BiOI/BiP_5O_{14}$ heterostructure (by adding 2% of NaH_2PO_4) were the main reactive species during the photocatalytic process, consisting with the above scheme of charge transfer and separation.

The intermediates of phenol degradation were examined LC-MS analysis. The mass spectra of products stemmed from the degraded phenol analyzed at different retention time (RT) were showed in Fig. S15. Then, the possible reaction pathways for phenol degradation by $Bi_4O_5I_2$-$BiPO_4$ nanosheets were proposed (Fig. 8). The main reactive species generated by the $Bi_4O_5I_2$-$BiPO_4$ nanosheets attack the benzene ring and oxidize phenolic hydroxyl groups though nucleophilic attack [52]. Then, the aromatic rings were opened gradually, forming small organic acids eventually and achieving oxidative mineralization of phenol.

The photocatalytic mechanism of the $BiOI/BiP_5O_{14}$ heterostructure driven by the internal electric field was illustrated in Fig. S16. During the photocatalytic process, the charge separation follows the Z-scheme that electrons from the CB of BiOI migrate to the VB of BiP_5O_{14}, remaining the electrons at CB of BiP_5O_{14} and holes at VB of BiOI [53,54]. Thus, the charge carriers could be separated and the recombination of charge carriers also can be suppressed efficiently. As driven by the internal electric field, the separated holes and electrons respective transfer to the surface of BiP_5O_{14} and BiOI directionally, participating the photocatalytic reaction of phenol. As a result, the photocatalytic performance and mineralization ability of phenol over the $BiOI/BiP_5O_{14}$ heterostructure were significantly promoted.

4. Conclusions

The $BiOI/BiP_5O_{14}$ heterostructure nanosheets were prepared through the epitaxial growth of BiP_5O_{14} layer on the surface of BiOI nanosheets. When adding 2% of NaH_2PO_4, the $BiOI/BiP_5O_{14}$ heterostructure nanosheets with BiP_5O_{14} monolayer and less defects could be produced. Furthermore, this $BiOI/BiP_5O_{14}$ heterostructure could establish strong interfacial internal electric field between each component. And the photogenerated holes and electrons transfer to the surface of BiP_5O_{14} and BiOI directionally. As a result, the reaction constant rates of this $BiOI/BiP_5O_{14}$ heterostructure nanosheets under full spectra and visible light were 0.292 h^{-1} and 0.260 h^{-1}, respectively, which was 9.6 times and 8.5 times higher than that of pristine BiOI nanosheets. Accordingly, its TOC removal rate also was 8.9 times higher that of BiOI nanosheets under full spectra.

CRediT authorship contribution statement

Zhaohui Wu: Design, Validation, Methodology, Data analysis, Writing – original draft, Writing – review & editing. **Jianfang Jing**: Visualization, Investigation. **Kungfeng Zhang**: Investigation. **Wenlu Li**: Visualization. **Jun Yang**: Visualization. **Jie Shen**: Visualization. **Shumin Zhang**: Investigation. **Kaiqiang Xu**: Investigation. **Shiying Zhang**: Supervision, Review, Funding acquisition. **Yongfa Zhu**: Overall supervision, Resources, Writing – review & editing.

Declaration of Competing Interest

The authors declare that they have no known competing financial interests or personal relationships that could have appeared to influence the work reported in this paper.

Acknowledgements

Appendix A. Supporting information

Supplementary data associated with this article can be found in the online version at doi:10.1016/j.apcatb.2022.121153.

References

[1] J. Li, X.Y. Wu, W.F. Pan, G.K. Zhang, H. Chen, Vacancy-rich monolayer BiO_{2-x} as a highly efficient UV, visible, and near-infrared responsive photocatalyst, Angew. Chem. Int. Ed. 57 (2018) 491–495.

[2] H. Miao, J. Yang, G.L. Peng, H.Q. Li, Y.F. Zhu, Enhancement of the degradation ability for organic pollutants via the synergistic effect of photoelectrocatalysis on a self-assembled perylene diimide (SA-PDI) thin film, Sci. Bull. 64 (2019) 896–903.

[3] J. Cao, B.Y. Xu, H.L. Lin, S.F. Chen, Highly improved visible light photocatalytic activity of $BiPO_4$ through fabricating a novel p-n heterojunction $BiOI/BiPO_4$ nanocomposite, Chem. Eng. J. 228 (2013) 482–488.

[4] Y. Peng, M. Yan, Q.G. Chen, C.M. Fan, H.Y. Zhou, A.W. Xu, Novel onedimensional Bi_2O_3-Bi_2WO_6 p-n hierarchical heterojunction with enhanced photocatalytic activity, J. Mater. Chem. A 2 (2014) 8517–8524.

[5] Y.J. Sun, J.Z. Liao, F. Dong, S.J. Wu, L.D. Sun, A $Bi/BiOI/(BiO)_2CO_3$ heterostructure for enhanced photocatalytic NO removal under visible light, Chin. J. Catal. 40 (2019) 362–370.

[6] R. Li, J.X. Liu, X.F. Zhang, Y.W. Wang, Y.F. Wang, C.M. Zhang, X.C. Zhang, C. M. Fan, Iodide-modified $Bi_4O_5Br_2$ photocatalyst with tunable conduction band position for efficient visible-light decontamination of pollutants, Chem. Eng. J. 339 (2018) 42–50.

[7] W.Y. Yan Chen, Shuang Gao, Linggang Zhu, Caixia Sun, Qi Li, Internal polarization modulation in Bi_2MoO_6 for photocatalytic performance enhancement under visible-light illumination, Chemsuschem 11 (2018) 1521–1532.

[8] S.Q. Guo, X.H. Zhu, H.J. Zhang, B.C. Gu, W. Chen, L. Liu, P.J.J. Alvarez, Improving photocatalytic water treatment through nanocrystal engineering: mesoporous nanosheet-assembled 3D BiOCl hierarchical nanostructures that induce unprecedented large vacancies, Environ. Sci. Technol. 52 (2018) 6872–6880.

[9] Y.F. Jia, S.P. Li, H. Ma, J.Z. Gao, G.Q. Zhu, F.C. Zhang, J.Y. Park, S. Cha, J.S. Bae, C. Liu, Oxygen vacancy rich Bi_2O_4-Bi_4O_7-BiO_{2-x} composites for UV–vis-NIR activated high efficient photocatalytic degradation of bisphenol A, J. Hazard. Mater. 382 (2020), 121121.

[10] Q. Wang, W. Wang, L.L. Zhong, D.M. Liu, X.Z. Cao, F.Y. Cui, Oxygen vacancy-rich 2D/2D $BiOCl$-g-C_3N_4 ultrathin heterostructure nanosheets for enhanced visible-light-driven photocatalytic activity in environmental remediation, Appl. Catal. B Environ. 220 (2018) 290–302.

[11] R.A. He, J.Q. Zhou, H.Q. Fu, S.Y. Zhang, C.J. Jiang, Room-temperature in situ fabrication of Bi_2O_3/g-C_3N_4 direct Z-scheme photocatalyst with enhanced photocatalytic activity, Appl. Surf. Sci. 430 (2018) 273–282.

[12] H.Y. Wu, X.M. Liu, H. Xu, X.M. Yang, J.H. Ye, Efficient photodegradation of 2-chloro-4-nitrophenol over Fe-doped BiOCl nanosheets with oxygen vacancy, Catal. Sci. Technol. (2021).

[13] Y. Chen, W.Y. Yang, S. Gao, L.G. Zhu, C.X. Sun, Q. Li, Internal polarization modulation in Bi_2MoO_6 for photocatalytic performance enhancement under visible-light illumination, Chemsuschem 11 (2018) 1521–1532.

[14] J.G. Sun, S.J. Wu, S.Z. Yang, Q. Li, J.W. Xiong, Z.Z. Yang, L. Gu, X.X. Zhang, L. D. Sun, Enhanced photocatalytic activity induced by sp^3 to sp^2 transition of carbon dopants in BiOCl crystals, Appl. Catal. B Environ. 221 (2018) 467–472.

[15] B. Sarwan, B. Pare, A.D. Acharya, Heterogeneous photocatalytic degradation of nile blue dye in aqueous BiOCl suspensions, Appl. Surf. Sci. 301 (2014) 99–106.

[16] D. Liu, W.Q. Yao, J. Wang, Y.F. Liu, M. Zhang, Y.F. Zhu, Enhanced visible light photocatalytic performance of a novel heterostructured $Bi_4O_5Br_2/Bi_{24}O_{31}Br_{10}/Bi_2SiO_5$ photocatalyst, Appl. Catal. B Environ. 172 (2015) 100–107.

[17] M. Sun, Q.Q. Wei, Y. Shao, B. Du, T. Yan, L.G. Yan, D.Z. Li, Engineering composition-tunable 3D hierarchical bismuth oxyiodides heterojunctions: Ionic liquid-assisted fabrication with strong adsorption ability and enhanced photocatalytic properties, Appl. Catal. B Environ. 233 (2018) 250–259.

[18] L. Liang, J. Cao, H.L. Lin, X.M. Guo, M.Y. Zhang, S.F. Chen, Synergetic effects of I-ions and BiOI on visible-light-activity enhancement of wide-band-gap $(BiO)_2CO_3$, Appl. Surf. Sci. 414 (2017) 365–372.

[19] Y. Mi, M. Zhou, L.Y. Wen, H.P. Zhao, Y. Lei, A highly efficient visible-light driven photocatalyst: two dimensional square-like bismuth oxyiodine nanosheets, Dalton Trans. 43 (2014) 9549–9556.

[20] C. Liu, X.J. Wang, Room temperature synthesis of $Bi_4O_5I_2$ and Bi_5O_7I ultrathin nanosheets with a high visible light photocatalytic performance, Dalton Trans. 45 (2016) 7720–7727.

[21] X. Xiao, C.L. Xing, G.P. He, X.X. Zuo, J.M. Nan, L.S. Wang, Solvothermal synthesis of novel hierarchical $Bi_4O_5I_2$ nanoflakes with highly visible light photocatalytic performance for the degradation of 4-tert-butylphe, Appl. Catal. B Environ. 148 (2014) 154–163.

[22] Y. Guo, W.X. Shi, Y.F. Zhu, Y.P. Xu, F.Y. Cui, Enhanced photoactivity and oxidizing ability simultaneously via internal electric field and valence band position by crystal structure of bismuth oxyiodide, Appl. Catal. B Environ. 262 (2020), 118262.

[23] Y.F. Liu, W.Q. Yao, D. Liu, R.L. Zong, M. Zhang, X.G. Ma, Y.F. Zhu, Enhancement of visible light mineralization ability and photocatalytic activity of $BiPO_4/BiOI$, Appl. Catal. B Environ. 163 (2015) 547–553.

[24] Y.F. Chen, J.Z. Fang, S.Y. Lu, W.C. Xu, Z. Liu, X.X. Xu, Z.Q. Fang, One-step hydrothermal synthesis of $BiOI/Bi_2WO_6$ hierarchical heterostructure with highly photocatalytic activity, J. Chem. Technol. Biot. 90 (2015) 947–954.

[25] C. Chang, L.Y. Zhu, S.F. Wang, X.L. Chu, L.F. Yue, Novel mesoporous graphite carbon nitride/BiOI heterojunction for enhancing photocatalytic performance under visible-light irradiation, ACS Appl. Mater. Inter. 6 (2014) 5083–5093.

[26] Q.B. Li, H. Qin, H.K. Zhao, X. Zhao, X.F. Cheng, W.L. Fan, Facile fabrication of a $BiOI/TiO_2$ p-n junction via a surface charge-induced electrostatic self-assembly method, Appl. Surf. Sci. 457 (2018) 59–68.

[27] J.J. Jiang, H.T. Wang, X.D. Chen, S. Li, T.F. Xie, D.J. Wang, Y.H. Lin, Enhanced photocatalytic degradation of phenol and photogenerated charges transfer property over BiOI-loaded ZnO composites, J. Colloid Interf. Sci. 494 (2017) 130–138.

[28] L.M. Sun, L. Xiang, X. Zhao, C.J. Jia, J. Yang, Z. Jin, X.F. Cheng, W.L. Fan, Enhanced visible-light photocatalytic activity of BiOI/BiOCl heterojunctions: key role of crystal facet combination, ACS Catal. 5 (2015) 3540–3551.

[29] X.Y. Kong, W.Q. Lee, A.R. Mohamed, S.P. Chai, Effective steering of charge flow through synergistic inducing oxygen vacancy defects and p-n heterojunctions in 2D/2D surface-engineered $Bi_2WO_6/BiOI$ cascade: towards superior photocatalytic CO_2 reduction activity, Chem. Eng. J. 372 (2019) 1183–1193.

[30] Y. Peng, P.P. Yu, H.Y. Zhou, A.W. Xu, Synthesis of $BiOI/Bi_4O_5I_2/Bi_2O_2CO_3$ p-n-p heterojunctions with superior photocatalytic activities, New J. Chem. 39 (2015) 8321–8328.

[31] J.J. Zhang, T. Wang, X.X. Chang, A. Li, J.L. Gong, Fabrication of porous nanoflake $BiMO_x$ (M = W, V, and Mo) photoanodes via hydrothermal anion exchange, Chem. Sci. 7 (2016) 6381–6386.

[32] L. Wang, K. Xu, W. Cui, D.D. Lv, L. Wang, L. Ren, X. Xu, F. Dong, S.X. Dou, W. C. Hao, Y. Du, Monolayer epitaxial heterostructures for selective visible-light-driven photocatalytic NO oxidation, Adv. Funct. Mater. 29 (2019), 1808084.

[33] Y.J. Wang, J.R. Jin, W.G. Chu, D. Cahen, T. He, Synergistic effect of charge generation and separation in epitaxially grown $BiOCl/Bi_2S_3$ nano-heterostructure, ACS Appl. Mater. Inter. 10 (2018) 15304–15313.

[34] Y. Min, G. Park, B. Kim, A. Giri, J. Zeng, J.W. Roh, S.I. Kim, K.H. Lee, U. Jeong, Synthesis of multishell nanoplates by consecutive epitaxial growth of Bi_2Se_3 and Bi_2Te_3 nanoplates and enhanced thermoelectric properties, ACS Nano 9 (2015) 6843–6853.

[35] Q. Wang, Z.Q. Liu, D.M. Liu, G.S. Liu, M. Yang, F.Y. Cui, W. Wang, Ultrathin two-dimensional $BiOBr_xI_{1-x}$ solid solution with rich oxygen vacancies for enhanced visible-light-driven photoactivity in environmental remediation, Appl. Catal. B Environ. 236 (2018) 222–232.

[36] Z.H. Wu, J. Shen, N. Ma, Z.F. Li, M. Wu, D.F. Xu, S.Y. Zhang, W.H. Feng, Y.F. Zhu, $Bi_4O_5Br_2$ nanosheets with vertical aligned facets for efficient visible-light-driven photodegradation of BPA, Appl. Catal. B Environ. 286 (2021), 119937.

[37] G. Kresse, J. Furthmüller, Efficiency of ab-initio total energy calculations for metals and semiconductors using a plane-wave basis set, Comp. Mater. Sci. 6 (1996) 15–50.

[38] J.P. Perdew, K. Burke, M. Ernzerhof, Generalized gradient approximation made simple, Phys. Rev. Lett. 77 (1996) 3865–3868.

[39] G. Kresse, J. Furthmüller, Efficiency of ab-initio total energy calculations for metals and semiconductors using a plane-wave basis set, Comp. Mater. Sci. 6 (1996) 15–50.

[40] J. Kresse, J. Hafner, Ab initio molecular-dynamics simulation of the liquid-metal-amorphous-semiconductor transition in germanium, Phys. Rev. B 49 (1994) 14251–14269.

[41] M.Z. Bellus, M. Li, S.D. Lane, F. Ceballos, Q.N. Cui, X.C. Zeng, H. Zhao, Type-I van der Waals heterostructure formed by MoS_2 and ReS_2 monolayers, Nanoscale Horiz. 2 (2017) 31–36.

[42] Z. Xing, J. Hu, M. Ma, H. Lin, Y.M. An, Z.H. Liu, Y. Zhang, J.Y. Li, S.H. Yang, From one to two: in situ construction of an ultrathin ^{2}D–^{2}D closely bonded heterojunction from a single-phase monolayer nanosheet, J. Am. Chem. Soc. 141 (2019) 19715–19727.

[43] G.Q. Zhang, L. Cai, Y.F. Zhang, Y. Wei, Bi^{5+}, $Bi^{(3−x)+}$, and oxygen vacancy induced $BiOCl_xI_{1−x}$ solid solution toward promoting visible-light driven photocatalytic activity, Chem. Eur. J. 24 (2018) 7434–7444.

[44] H. Li, J. Shang, H.J. Zhu, Z.P. Yang, Z.H. Ai, L.Z. Zhang, Oxygen vacancy structure associated photocatalytic water oxidation of BiOCl, ACS Catal. 6 (2016) 8276–8285.

[45] L. Wang, D.D. Lv, F. Dong, X.L. Wu, N.Y. Cheng, J. Scott, X. Xu, W.C. Hao, Y. Du, Boosting visible-light-driven photo-oxidation of BiOCl by promoted charge separation via vacancy engineering, ACS Sustain. Chem. Eng. 7 (2019) 3010–3017.

[46] Y.H. Kim, S.Y. Lee, H. Umh, H.D. Song, J.W. Han, J.W. Choi, J. Yi, Directional change of interfacial electric field by carbon insertion in heterojunction system TiO_2/WO_3, ACS Appl. Mater. Inter. 12 (2020) 15239–15245.

[47] Z.J. Zhang, X.J. Chen, H.J. Zhang, W.X. Liu, W. Zhu, Y.F. Zhu, A highly crystalline perylene imide polymer with the robust built-in electric field for efficient photocatalytic water oxidation, Adv. Mater. 32 (2020), 1907746.

[48] Y. Yang, F. Teng, Y.D. Kan, L.M. Yang, Z.L. Liu, W.H. Gu, A. Zhang, W.Y. Hao, Y. R. Teng, Investigation of the charges separation and transfer behavior of BiOCl/ BiF_3 heterojunction, Appl. Catal. B Environ. 205 (2017) 412–420.

[49] X.J. Chen, J. Wang, Y.Q. Chai, Z.J. Zhang, Y.F. Zhu, Efficient photocatalytic overall water splitting induced by the giant internal electric field of a g-C_3N_4/rGO/PDIP Z-scheme heterojunction, Adv. Mater. 33 (2021), 2007479.

[50] S. Liu, M.Y. Zhao, Z.T. He, Y. Zhong, H. Ding, D.M. Chen, Preparation of a p-n heterojunction 2D BiOI nanosheet/1D $BiPO_4$ nanorod composite electrode for enhanced visible light photoelectrocatalysis, Chin. J. Catal. 40 (2019) 446–457.

[51] O. Amiri, F. Beshkar, S.S. Ahmed, P.H. Mahmood, A.A. Dezaye, Hierarchical p-BiOI/n-$BiPO_4$ heterojunction nanocomposite with enhanced visible-light photocatalytic desulfurization of thiophene under mild conditions, Int. J. Hydrog. Energy 46 (2021) 6547–6560.

[52] S. Meshrama, R. Limaye , S. Ghodke, S. Nigam, S. Sonawane, R. Chikate, Continuous flow photocatalytic reactor using ZnO–bentonite nanocomposite for degradation of phenol, Chem. Eng. J. 172 (2011) 1008–1015.

[53] Y.F. Jia, S.P. Li, J.Z. Gao, G.Q. Zhu, F.C. Zhang, X.J. Shi, Y. Huang, C.L. Liu, Highly efficient $(BiO)_2CO_3$-$BiO_{2−x}$-graphene photocatalysts: Z-Scheme photocatalytic mechanism for their enhanced photocatalytic removal of NO, Appl. Catal. B Environ. 240 (2019) 241–252.

[54] Y. Chen, F. Wang, Y.H. Cao, F.Y. Zhang, Y.Z. Zou, Z.A. Huang, L.Q. Ye, Y. Zhou, Interfacial oxygen vacancy engineered two-dimensional g-C_3N_4/BiOCl heterostructures with boosted photocatalytic conversion of CO_2, ACS Appl. Energ. Mater. 3 (2020) 4610–4618.